Article

Microstructural Evolution of Irradiated Cr-Coated Zr-4 under In Situ Transmission Electron Microscopy Heating

Yuxin Zhong [1], Xiaoyong Wu [2], Lu Wu [3], Sha Zhao [1], Hanxuan Su [1], Zhien Ning [3], Wei Zhang [3], Ning Liu [1] and Jijun Yang [1,*]

[1] Key Laboratory of Radiation Physics and Technology of Ministry of Education, Institute of Nuclear Science and Technology, Sichuan University, Chengdu 610044, China; wthxy34@163.com (Y.Z.)
[2] Laboratory of science and Technology on Reactor Fuel and Materials, Nuclear Power Institute of China, Chengdu 610213, China
[3] The First Sub-Institute, Nuclear Power Institute of China, Chengdu 610213, China
[*] Correspondence: jjyang@scu.edu.cn

Abstract: The structural evolution of Cr-coated Zr-4 after irradiation was studied via in situ TEM in the temperature range from room temperature to 1000 °C. The results show that the krypton bubbles appeared at ~700 °C, and their size increased with increasing temperatures. The grain size and shape of the irradiated Zr-4 substrate changed with increasing temperature, and finally, columnar crystals appeared, which was related to the compressive stress induced via irradiation. The Cr_2Zr C14 phases formed at both the interface and the substrate at 700 °C and 1000 °C. Moreover, the accelerated failure process of irradiated Cr coating at high temperatures was observed via in situ TEM analysis.

Keywords: ion irradiation; high temperature; in situ TEM; interface

1. Introduction

Cr coatings have been widely studied in the nuclear research community [1–8] for their great performance, including good oxidation resistance [9–12], high coating–substrate adhesion strength [13], and lower thermal neutron absorption cross-section. The application of the Cr coating in the nuclear field has two aspects: ATF (accident–tolerant fuel) cladding coatings and diffusion barrier coatings in the ATF pellet. For the latter, to improve the fuel thermal conductivity and block the fission products release, micro-cell UO_2 pellets with metal cell walls (such as Cr, Mo, and W) were suggested by the Korea Atomic Energy Research Institute (KAERI) [14–18]. Cr coating was studied for use in the inner surface of the cladding as a diffusion barrier layer between the fuel core and the cladding. To further study the applicability of Cr coating as a diffusion barrier layer, Cr-coated Zr-4 was selected. However, many defects in the interface will deteriorate the coating service performance. Notably, in the complex service environments of a reactor, an operation (such as high temperatures and irradiation [19]) could accelerate the coating failure via the influence of the structure and chemical composition at the interface. In particular, the interface is critical for coating to survive in various environments.

Regarding the influence of temperature, many studies demonstrated that the phenomenon of structural and composition change in Cr-coated Zr-4 was found at high temperatures, such as phase transition in the substrate, element interdiffusion [20,21], grain coarsening, and void and intermetallic layer generations [22]. Huang et al. [23] indicated that the microstructure of the Zr-4 alloy substrate changed via recrystallization at high temperatures, and an intermetallic layer of Cr_2Zr was formed. Jiang et al. [20,24] indicated that high temperatures caused the crystallizing morphology of the Cr coating to change from columnar grains to equiaxial grains. Simultaneously, grain coarsening and a brittle intermetallic $ZrCr_2$ layer formed at the interface, which easily cracked under stress.

Wei et al. [25] found that interdiffusion occurred between Cr coating and Zr-4 at high temperatures, and the diffusion layer acted as the bonding layer between them.

Regarding the influence of irradiation, countless studies demonstrated irradiation-induced defects [26–29], accelerated diffusion [30], induced swelling and hardening, and misoriented Cr-Zr interfaces. Wu et al. [31] found that misoriented interfaces of Cr-Zr and the $Zr(Fe, Cr)_2$ C15 phases disappear after irradiation. Kuprin et al. [26,32] indicated that irradiation induced swelling in the Cr coating, and the degree of swelling increased as the irradiation temperature increased. Jiang et al. [27] found that irradiation introduced defects such as dislocation loops and simultaneously induced hardening in the samples. Jiang et al. [19] found that ion irradiation led to dislocation loops, a disorder region, and an amorphization region formed in Zr-4 and induced Zr-4 hardening by introducing the high density of point defects. However, there is little research on temperature influence in the Cr-Zr interface after irradiation, and it is necessary to study the irradiated Cr-Zr interface evolution under high temperatures for the commercial application of Cr coating. Thus, the relationship between the interface evolution and the coating failure under multi-field synergy should be researched in the future.

In this study, the influence of high temperatures on the microstructural evolution of the Cr-Zr interface after irradiation was investigated in situ. The Kr^+ and Mo^+ ion irradiation was used to pre-introduce damage in the Cr-coated Zr-4 before the in situ heating test. Kr^+ irradiation was selected to simulate the damage of fission gas to the inner surface coating of the cladding and its interface, while Mo^+ was selected to simulate the irradiation defect introduced via irradiation. Transmission electron microscopy (TEM) with energy-dispersive spectroscopy (EDS) was used to observe the microstructural evolution of the Cr-Zr interface with an increasing temperature (RT to 1000 °C). This study provides in situ observations of the research data for the Cr-Zr interface behaviors under both irradiation and high temperatures. The purpose of this work is to study the morphological changes in the Cr-Zr interface during continuous heating after irradiation damage and to further study the applicability of Cr coating as a diffusion barrier layer between fuel pellets and zircaloy cladding. The novelty of this work lies in the observation of the morphological changes in the Cr-Zr interface damaged via irradiation during continuous heating via TEM, and the observation of high-temperature recrystallization into columnar growth mode caused by introducing compressive stress via irradiation-induced defects.

## 2. Experimental

2.1. Coating Deposition

The Cr coatings were deposited on the Zr-4 substrate ($10 \times 10 \times 1.5$ mm^3) using pulsed biased multi-arc ion plating (Chengdu Qixing Vacuum Coating Technology Co., Ltd., Chengdu, China). The background vacuum was 5×10^{-3} Pa, and the targets were sputtered for 10 min with Ar^+ ions to remove the oxides and impurities on the target surface under an arc current of 90 A and a working pressure of 0.6 Pa. Subsequently, the sample surface was anti-sputtered for 10 min with the negative bias voltage of 400 V under a pressure of 2 Pa to remove the oil stains, oxides, etc.

The Cr coating with a thickness of approximately 6μm was deposited on the Zr-4 using a Cr target with φ100 mm in diameter (purity > 99.95%) under an arc current of 60 A, a negative substrate bias voltage of 100 V, and a 0.5 Pa argon atmosphere. In addition, the chamber temperature remained at 350 °C during the deposition process for 2 h. Cr was purchased from Zhong Nuo Advanced Material (Beijing) Technology Co., Ltd., Beijing, China.

2.2. Ion Irradiation

The Kr^+ ion beam was used on the irradiated sample cross-section at room temperature with an energy of 160 keV and an irradiation fluence of 8×10^{15} Kr/cm^2, and the Mo^+ ion beam at room temperature with an energy of 400 keV and an irradiation fluence of 4×10^{15} Mo/cm^2. Before ion irradiation, the SRIM 2013 software (the quick damage mode,

2013) was applied to simulate the Kr$^+$ and Mo$^+$ ions–irradiated Cr-coated Zr-4 to calculate the irradiation doses (in dpa), irradiation depth, and other relevant data, as shown in Figure 1. The mean displacement threshold energies of Cr and Zr used in this study are both 40 eV.
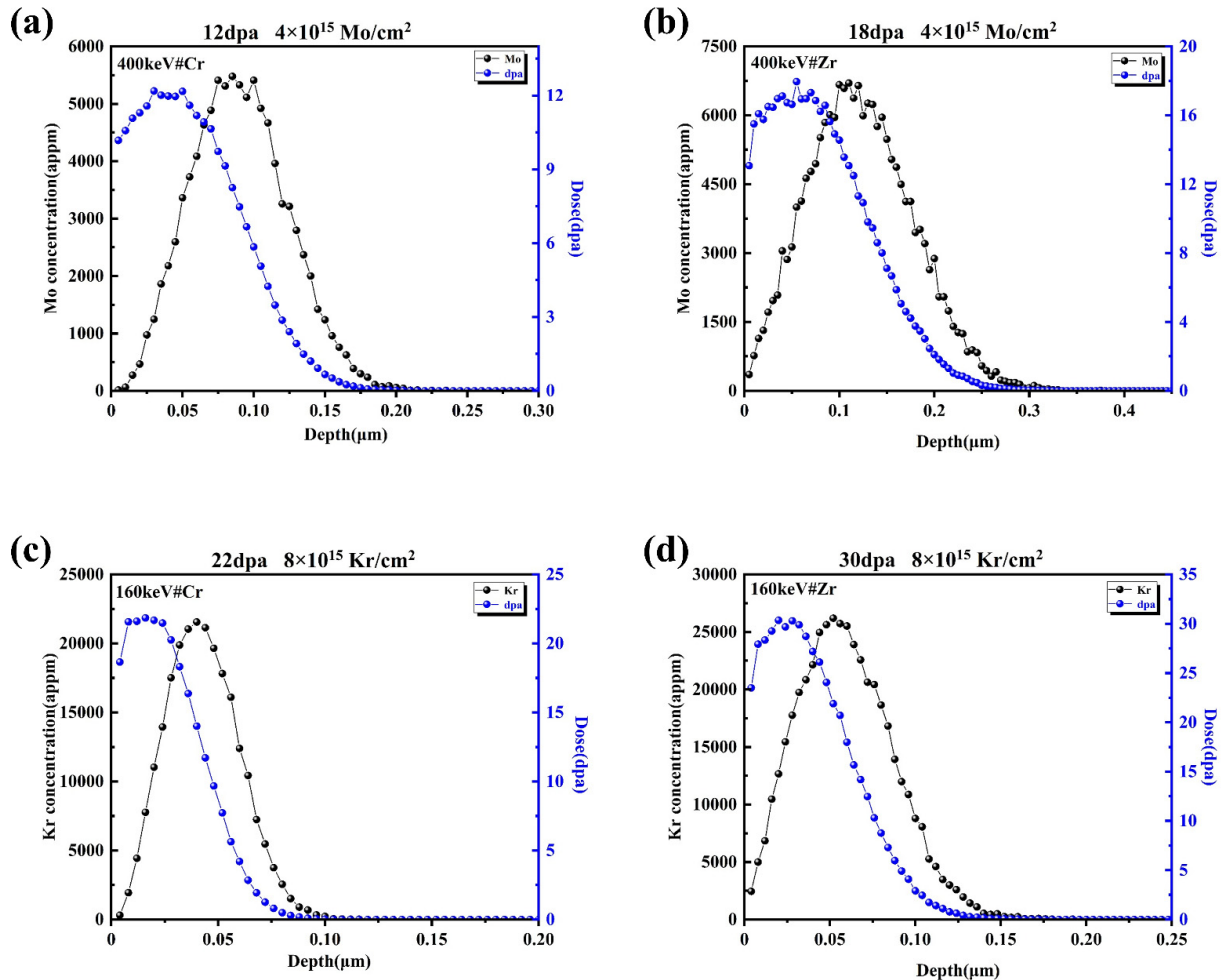
Figure 1. The depth distribution of the damage and concentration was calculated using SRIM 2013 with Mo$^+$ (400 keV, 4×10^{15} Mo/cm^2) and Kr$^+$ (160 keV, 8×10^{15} Kr/cm^2) ion irradiation.

In the simulated calculation (Figure 1), the extreme irradiation depth of the Kr$^+$ ion beam is ~100 nm in the Cr coating with irradiation doses of 22 dpa, whereas the irradiation depth is ~150 nm in the Zr-4 substrate with the irradiation doses of 30 dpa. Meanwhile, the Mo$^+$ ion irradiation is ~200 nm with 12 dpa in the Cr coating and ~300 nm with 18 dpa in the Zr-4 substrate.

2.3. Coating Characterization

The phase structure of the Cr coating was analyzed using an X-ray diffraction instrument (XRD, DX-2700BH, Dandong Haoyuan Instrument Co., Ltd., Dandong, China). Cu radiation is employed in X-ray diffraction experiments. The surface morphologies of the Cr coating were characterized using field emission scanning electron microscopy (FESEM, FEI Inspect F50, FEI, Hillsboro, OR, USA) with an energy dispersion spectrometer.

2.4. In Situ TEM Heating

The focus ion beam (FIB, FEI Helios Nano Lab 600i) device was used to cut the sample cross-section of the heavy-ion irradiation into the size required for the TEM ($3 \times 3 \times 0.07$ μm). Transmission electron microscopy (TEM, FEI Talos F200X) was applied

to characterize the microstructural evolution of Cr-coated Zr-4 in situ under increasing temperature, and the accelerating voltage is 200 kV. The number of electrons shot via electron guns per second is ~3.75×10^{13}. The sample was placed in an in situ heating mono-tilt rod and started at room temperature with a heating rate of 5 °C/s. The temperature changes over time during the in situ heating test are shown in Figure 2. The surface morphologies and microstructure of the sample were photographed at room temperature (RT) and after 20 min of heat preservation at 400 °C, 700 °C, and 1000 °C, respectively. The microstructural evolutions of the Zr-4 substrate, Cr coating, and interface were obtained to analyze the irradiation and temperature-cooperated influence on the Cr-coated Zr-4 interface.
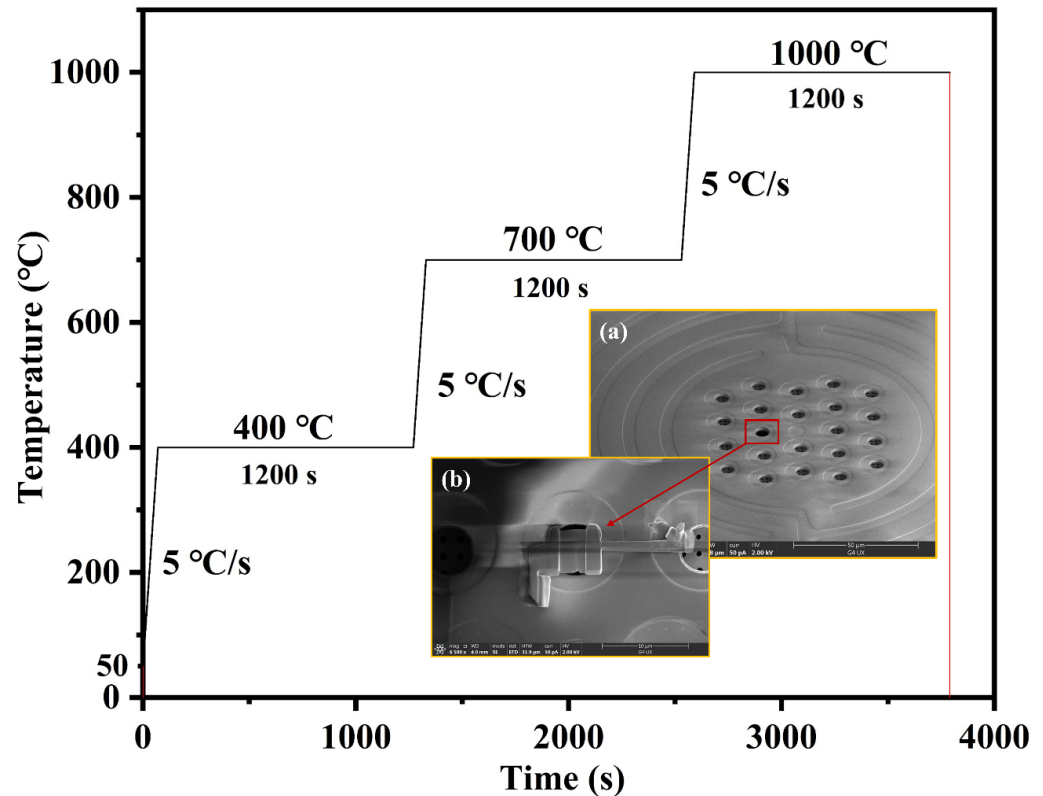

Figure 2. TEM in situ heating profile (the relationship between temperature and time): (**a**) the in situ heating sample holder and (**b**) the sample.

3. Results and Discussion

3.1. The Surface Morphologies and Microstructure of the Cr Coating in Deposition

The TEM image (Figure 3a) of the as-deposited Cr coating illustrates that Cr coating on Zr-4 substrate is grown to columnar crystals, and the SAED image (Figure 3b) indicates that the lattice type of Cr coating is body-centered cubic (BCC). The SAED image (Figure 3c) indicates that the lattice type of the Zr-4 substrate is hexagonal close-packed (HCP).

The XRD pattern of the as-deposited Cr coating, as seen in Figure 4c, indicates that the crystal orientation Cr (200) is the preferred orientation. The surface and cross-sectional morphologies of the as-deposited Cr coating are shown in Figures 4a and 4b, respectively, indicating that the Cr coating has a dense microstructure without voids and cracks but a few Cr metal melt droplets with a diameter < 2 μm on the Zr-4 substrate surface, which is caused by the multi-arc ion plating. In addition, the Cr coating has no obvious layering phenomenon and well binding on Zr-4 observed from the image of the cross-section (Figure 4b).
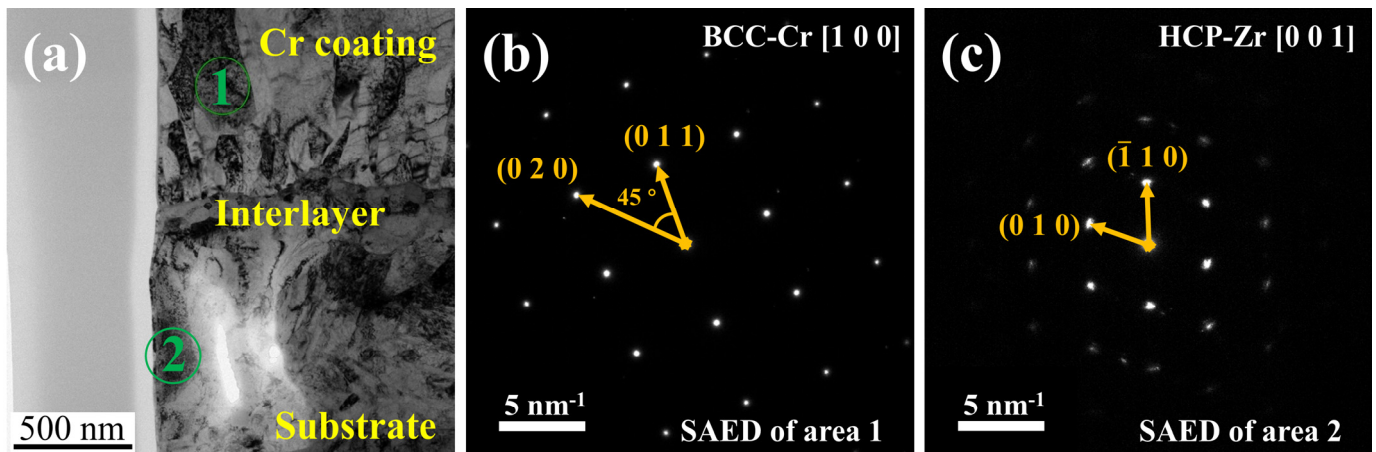
Figure 3. (**a**) Cross-section TEM micrographs of Cr-coated Zr-4; (**b**) SAED of the selected zone in the as-deposited Cr coating, as framed with green dotted ① in (**a**); (**c**) SAED of the selected zone in the Zr-4 substrate, as framed with green dotted ② in (**a**).
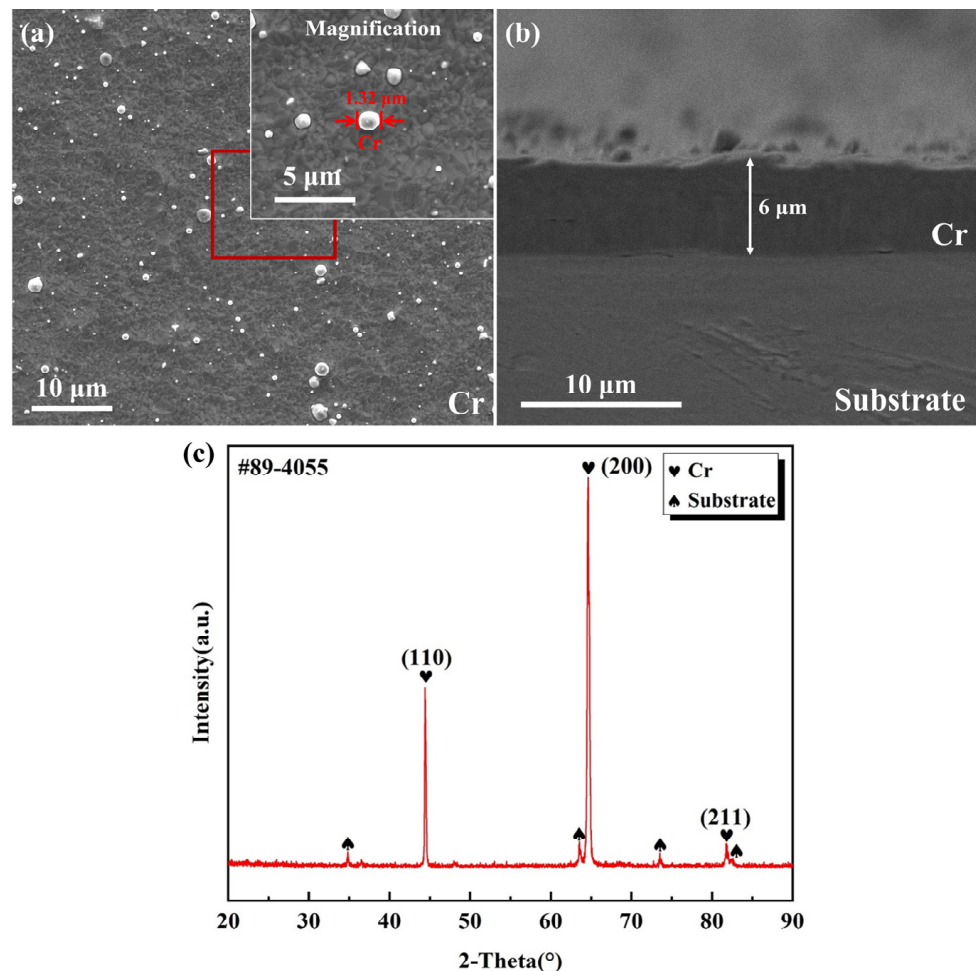
Figure 4. Surface (**a**) and cross-section (**b**) morphologies of an as-deposited Cr coating; (**c**) XRD of an as-deposited Cr coating.

3.2. Microstructure Evolution of Cr Coating

As shown in Figures 5b,d and 6d,i, some defects were observed in the irradiation region, such as the edge dislocations introduced via coating preparation. Some defects disappear with increasing temperature, which is due to the defects migrating to the grain

boundary and annihilating eventually. However, some defects grow due to the energy provided by high temperatures. As the temperature increases, the grain shape changes from columnar crystals to equiaxed grains (Figure 5i). The abnormal grain growth in the Cr coating is observed, which could be caused by the high local grain boundary mobility at high temperatures. Moreover, large numbers of cavities appear in the Cr coating (Figure 5f–h), most of which appear at the grain boundary; the reason could relate to atomic migration, grain boundary merger, vacancy aggregation growth, and then result in a certain effect on Cr coating failure.
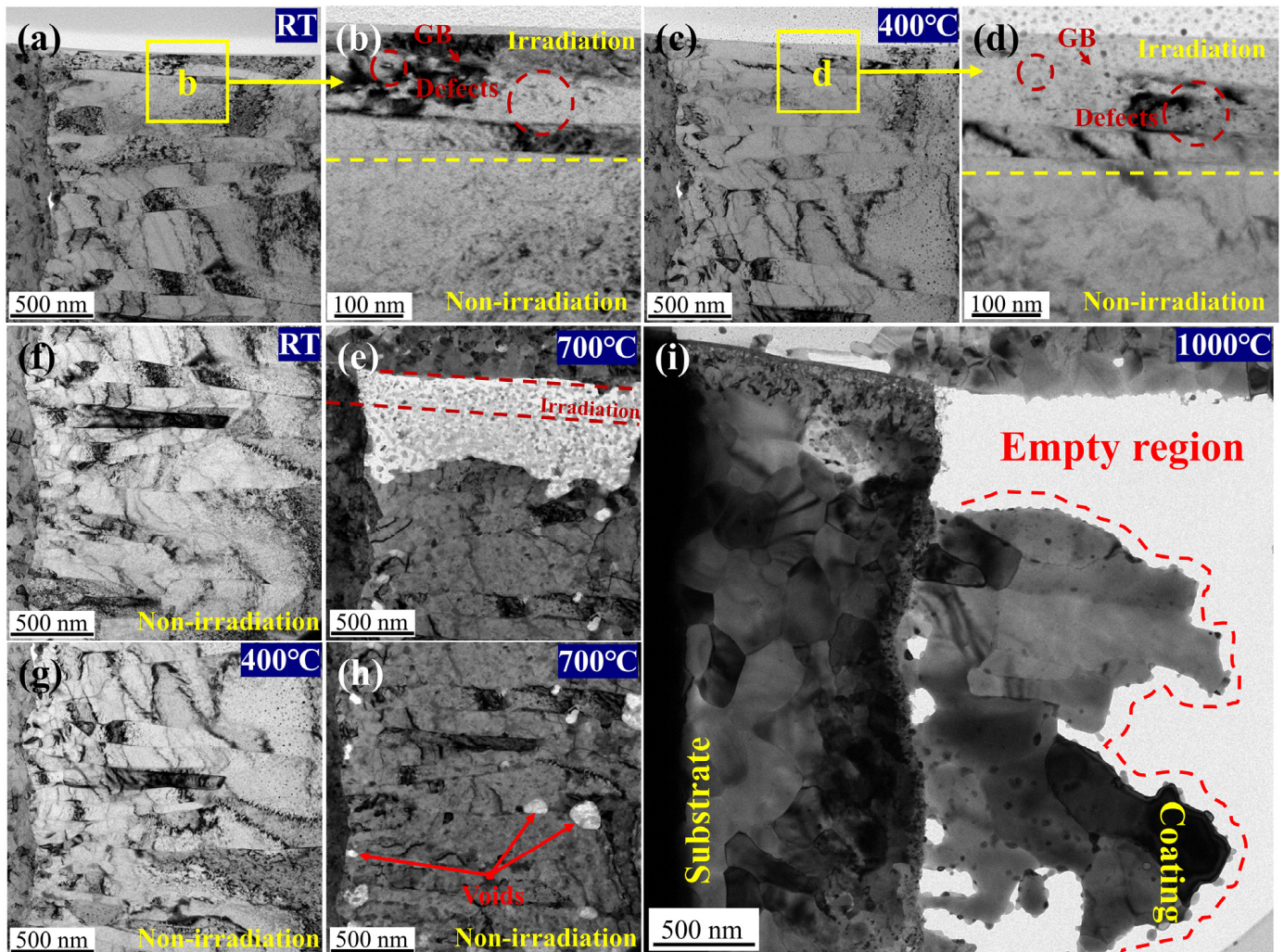

Figure 5. BF of Cr coating under different temperatures: (**a**,**b**,**f**) RT; (**c**,**d**,**g**) 400 °C; (**e**,**h**) 700 °C; and (**i**) 1000 °C. Above the yellow dotted line is the irradiated area, and below is the unirradiated area.

The Cr coating without phase transition in the entire in situ TEM heating test (Figure 6c,e,h,j), i.e., the body-centered cubic (BCC) structure, has been maintained. The lattice parameters of the Cr coating increase due to high temperatures, indicating that lattice expansion occurs at 1000 °C. In addition, the Cr element of the coating region significantly spreads outward with voids appearing beginning at ~700 °C. These voids gradually expand and eventually result in a spall of partial coating. It is due to the protective layer applied to the sample surface when performing a focused ion beam (FIB), and then, Cr spreads into the protective layer.
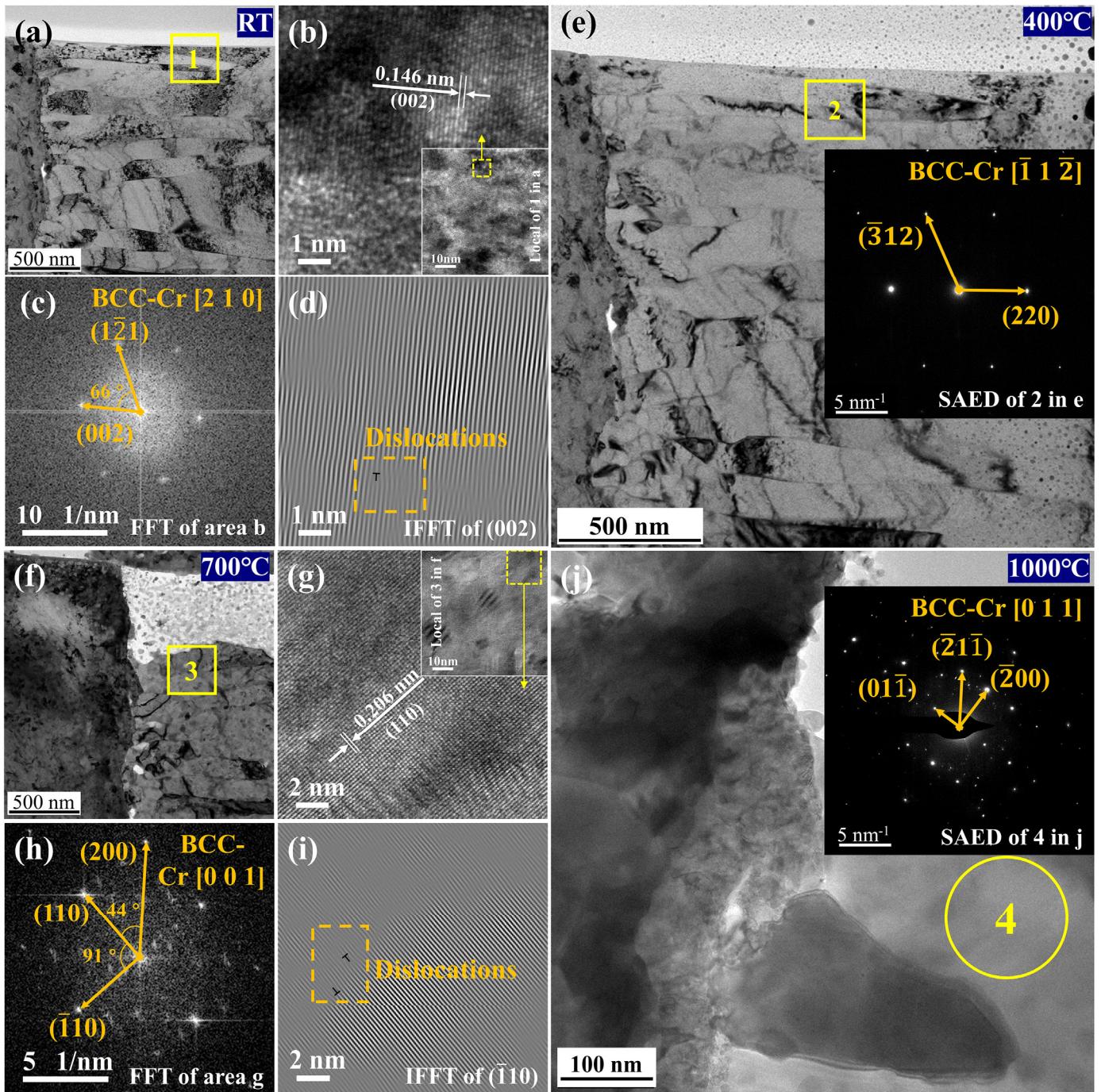
Figure 6. HRTEM and SAED of Cr coating under different temperatures: (**a–d**) RT; (**e**) 400 °C; (**f–i**) 700 °C; and (**j**) 1000 °C. Among them, **b–d** are the high-resolution observation and FFT results of region 1 in **a**; The SAED in **e** is the electron diffraction pattern of region 2 in **e**; **g–i** are the high-resolution observation and FFT results of region 3 in **f**; The SAED in **j** is the electron diffraction pattern of region 4 in **j**.

As shown in Figure 7, the failure degree of Cr coating after irradiation is higher than the unirradiated one at the same temperature and preservation time. It could be related to the irradiation-induced defects, and more element diffusion channels were provided by the defects at the irradiation region [30].
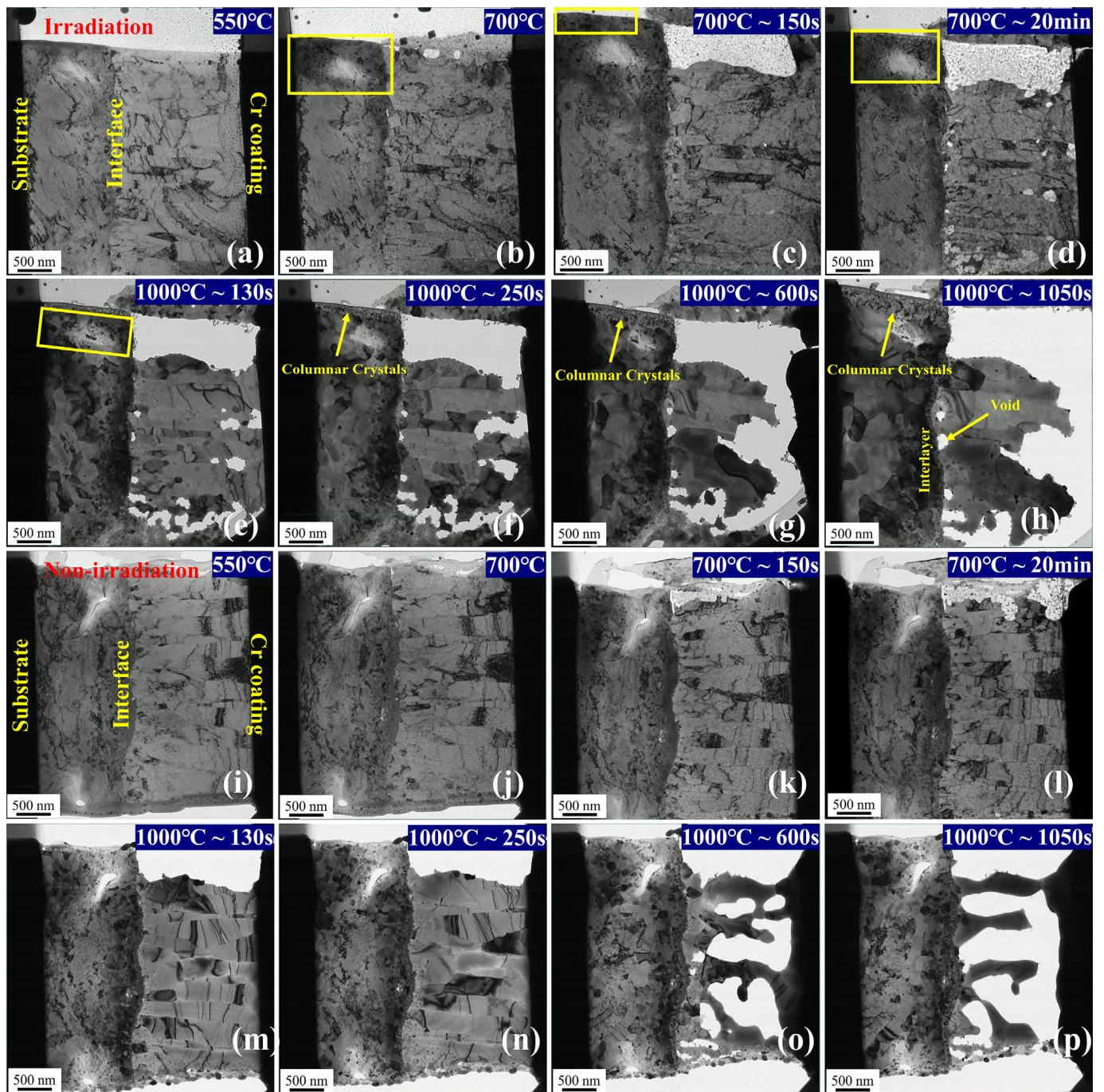
Figure 7. Morphology evolution of Cr-Zr with temperature and time increasing: (**a**–**h**) irradiation and (**i**–**p**) unirradiated (from the video). Moreover, (**a**–**d**) from video 2, (**e**–**h**) from video 3, (**i**–**l**) from video 5, and (**m**–**p**) from video 6 further show the morphology evolution. The yellow box area is the morphological change of the irradiated area observed with increasing temperature.

3.3. Microstructure Evolution of Zr-4 Substrate

A large number of pits in the cross-section of Zr-4 were observed (Figure 8b), which were not present before irradiation; the reason should be the ion irradiation sputtering effect [33]. A part of the atoms first collided out of their original lattice site and left vacancies, i.e., the primary knock-on atom (PKA), when high-energy ions bombarded Zr-4. On the other hand, a part of the atoms acquired collision energy via the interaction between high-energy ions and the lattice. Then, the atoms in Zr-4 left their original lattice site and

escaped from the surface once the collision energy over the threshold displacement energy formed pits on the surface via a defect reaction.
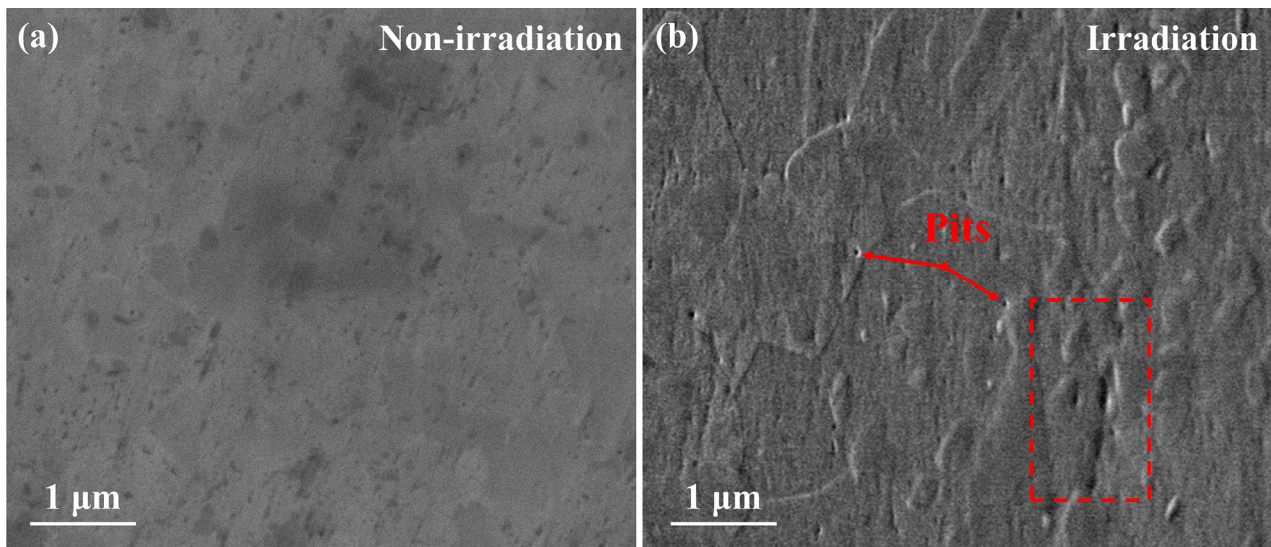

Figure 8. SEM of cross-section morphologies in Zr-4: (**a**) reference and (**b**) after Kr^+ and Mo^+ ion irradiation.

We observed that the Cr_2Zr intermetallic phase existed at 700 °C (Figure 9l) and 1000 °C (Figure 9m. SAED of Zr-4), which is due to the Cr atom diffusion to Zr-4 (Figure 9d,h,k). Meanwhile, the phase of Zr-4 changed from α-Zr (hcp) to β-Zr (bcc) at temperatures between 700 °C and 1000 °C (Figure 9c,g,l,m). The defect generated via ion irradiation caused the compressive stress, leading to the crystal plane spacing of the β-Zr decreased in its entirety. In addition, the larger the crystal plane index, the more decreased the crystal plane spacing was, which coincided with the phenomenon for the formed columnar crystal at 1000 °C (region 2 in Figure 10d).

The irradiation region of the substrate was eventually divided into two different regions by grain size. As shown in Figure 10c,d, the grain size of region 1 is smaller and had Kr^+ and Mo^+ ion irradiation with more irradiation damage, whereas the grain size of region 2 is larger without Kr^+ ion irradiation, which grew in the form of columnar crystals (i.e., no formation of krypton bubbles in region 2). There are many defects in region 1 (Figure 10d) of Zr-4. Initially, in the Zr-4 induced via cascading collision under Kr^+, Mo^+ ion irradiation (e.g., vacancy and point defect) should occur.

In Figure 10d, bubbles were observed in the surface region under ion irradiation at high temperatures, which formed via Kr^+ ion, and the krypton bubbles also caused grain refinement. One possibility is that electrons were captured via Kr^+ ions during the incident process; then, Kr atoms were formed. Subsequently, the krypton bubbles formed due to the Kr atoms stranded in the lattice and combined with vacancy clusters, which introduced the defects and caused further lattice distortions, resulting in grain refinement and stress generation [34]. In addition, krypton atoms combined with a vacancy or a vacancy cluster to form bubbles possibly relieve the stress generated via inserted atoms, and it is worth noting that the surface, as strong sinks for the defects, can absorb large numbers of interstitials, resulting in the unbalanced vacancy concentration between the surface and near-surface region; thus, most Kr bubbles accumulated in the near-surface region [35]. The vacancy introduced via irradiation also migrated and aggregated to dislocations, which, as a defect sink, led to Kr bubbles forming [33]. The krypton bubbles in the near-surface layer had an obvious accumulation and growth phenomenon at both 700 °C (Figure 10c) and 1000 °C (Figure 10d), where the yellow line in Figure 10c was the peak region (~60 nm) of the Kr^+ ion concentration in Zr-4. There was no additional irradiation damage generation or

injection of Kr⁺ ions in the whole in situ TEM heating process. Thus, the bubbles were most likely to grow due to migration and coalescence with the temperature increasing [36].
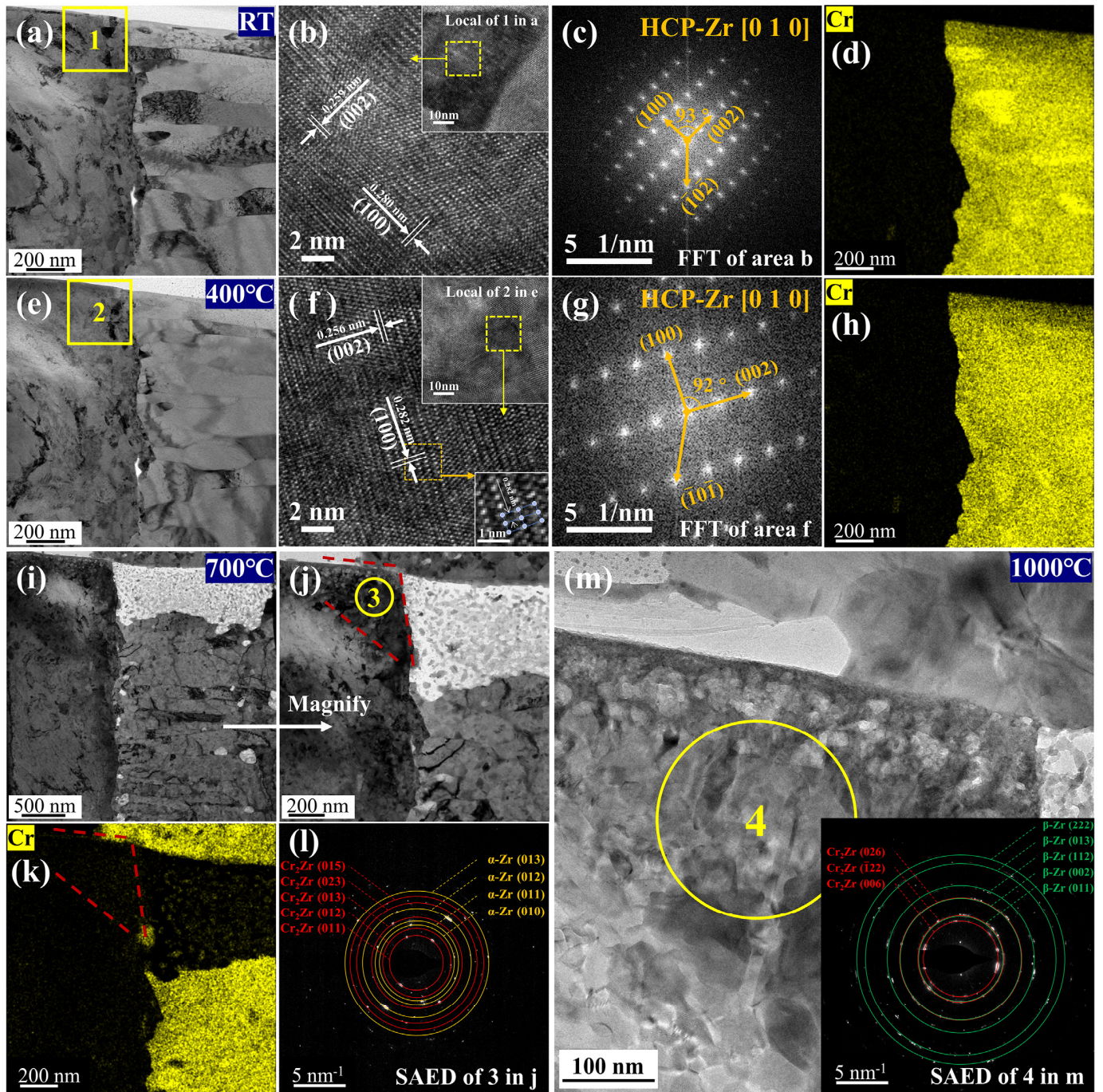
Figure 9. Microstructural evolution of Zr-4 under different temperatures: (**a**–**c**) RT; (**e**–**g**) 400 °C; (**i**,**j**,**l**) 700 °C; (**m**) 1000 °C; (**d**) EDS maps of Cr-coated Zr-4 in RT; (**h**) EDS maps of Cr-coated Zr-4 in 400 °C; and (**k**) EDS maps of Cr-coated Zr-4 in 700 °C. Among them, **b** and **c** are the high-resolution observation and FFT results of region 1 in **a**; **f** and **g** are the high-resolution observation and FFT results of region 2 in **e**; **l** is the electron diffraction pattern of region 3 in **j**; The SAED in **m** is the electron diffraction pattern of region 4 in **m**.
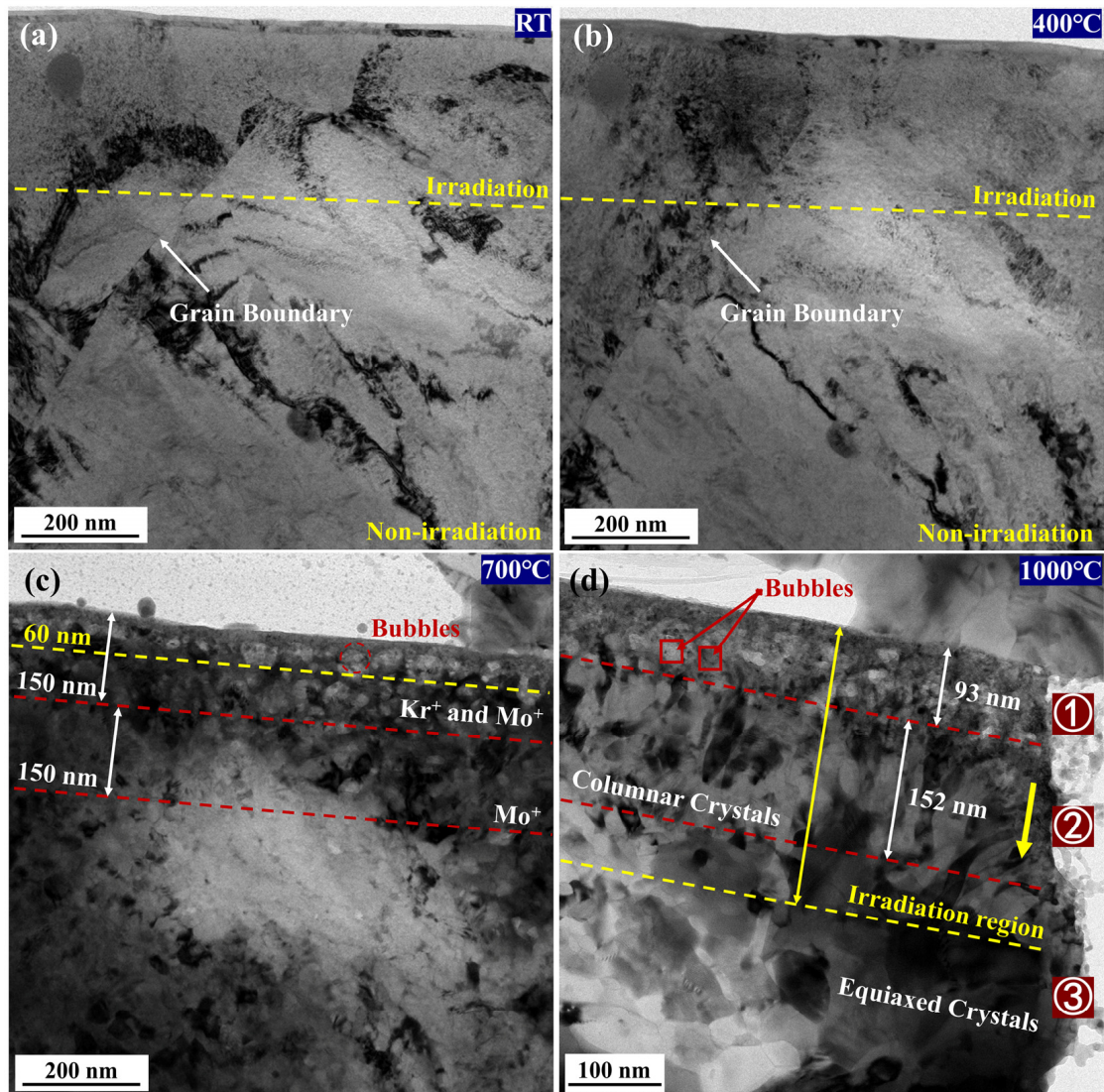
Figure 10. Bright field of Zr-4 under different temperatures: (**a**) RT; (**b**) 400 °C; (**c**) 700 °C; and (**d**) 1000 °C. Region 1 is the Kr^+ and Mo^+ irradiated area; Region 2 is the Mo^+ irradiated area; Region 3 is unirradiated area.

In the irradiation region of Zr-4 (Figure 10c), some point defects introduced via ion irradiation were used as nucleation sites, then grown under the action of the high temperature and energy of ion irradiation, which is the growth driver, and gradually formed plentiful grains, resulting in grain refinement. Meanwhile, accompanied by grain boundary disappearance (Figure 10a–c) and the stress generated, others were migrated to defect sinks, such as dislocations at high temperatures, and eventually annihilated. In addition, the thermal stress generated via ion irradiation also induces thermal recovery, and the results in the defects annihilated with dislocation density decrease, which promotes grain growth to a certain degree [34]. The phenomenon of grain size increase (equiaxed crystals) was observed in the unirradiated region of Zr-4 (region 3), which is because high temperatures provide energy for grain growth.

From video 2 and video 3 (Figure 7), it was observed that the irradiation region of Zr-4 began to change in morphology at 550 °C and grain refined after preservation at 700 °C for about 150 s; this stage could be related to the formation of the Cr_2Zr intermetallic phase and krypton bubbles. We observed the phenomenon of grain coarsening at 1000 °C followed by refinement with the shape of the columnar crystal. Two stages of the grain growth in Zr-4 (region 2) were divided using video 2 and video 3 (Figure 7a–h) when preservation

was at 1000 °C: (1) large numbers of fine grains grow at high temperature, and the grain boundaries merge to form equiaxed crystals with larger grain size; (2) with the prolongation of the preservation time, column crystals with smaller grain size were gradually formed along the direction of the yellow arrow (Figure 10d). The high temperatures providing the energy for grain growth is the reason for the first stage, while the second stage could be related to the sample size and the stress generated in the irradiation region. The sample size is very small and close to the two-dimensional material; thus, there was a longitudinal stress constraint (vertical to the sample plane orientation) when the atoms migrated, resulting in lateral growth (along the sample plane orientation), and the defects due to irradiation could lead to the anisotropy stresses at the migration of atoms or defects (region 2 coincides with the range of Mo^+ ion irradiation) and finally growth to form columnar crystals with a clear grain boundary, rather than equiaxed crystals.

In summary, ion irradiation-induced defects (e.g., edge dislocation, bubbles, and so on), recovery, recrystallization, and grain coarsening at high temperatures result in grain size changes, and the phase transition at high temperatures caused the lattice parameter changes in the Zr-4, thus affecting the substrate–coating bonding strength. Subsequently, the phenomena of lattice distortion and atomic misalignment will lead to coating failure in severe cases.

However, a series of irradiation effects due to ion irradiation (e.g., grain refinement, irradiation swelling, irradiation-induced defects, and so on) and the impact and extent of the synergistic effect of ion irradiation and high temperatures on element diffusion still need further research.

3.4. Microstructure and Morphological Evolution of Cr-Zr Interlayer

We observed that the Cr_2Zr (C14, hcp) intermetallic phase generated at both 700 °C and 1000 °C (Figure 11f,h), which caused a certain volume expansion (the volume expansion coefficient of Cr atoms to Cr_2Zr = 1.9) [21], whereas the lattice parameters generated via Cr_2Zr at the two temperatures are slightly different. The lattice parameters and space groups of the aforementioned compounds are as follows:
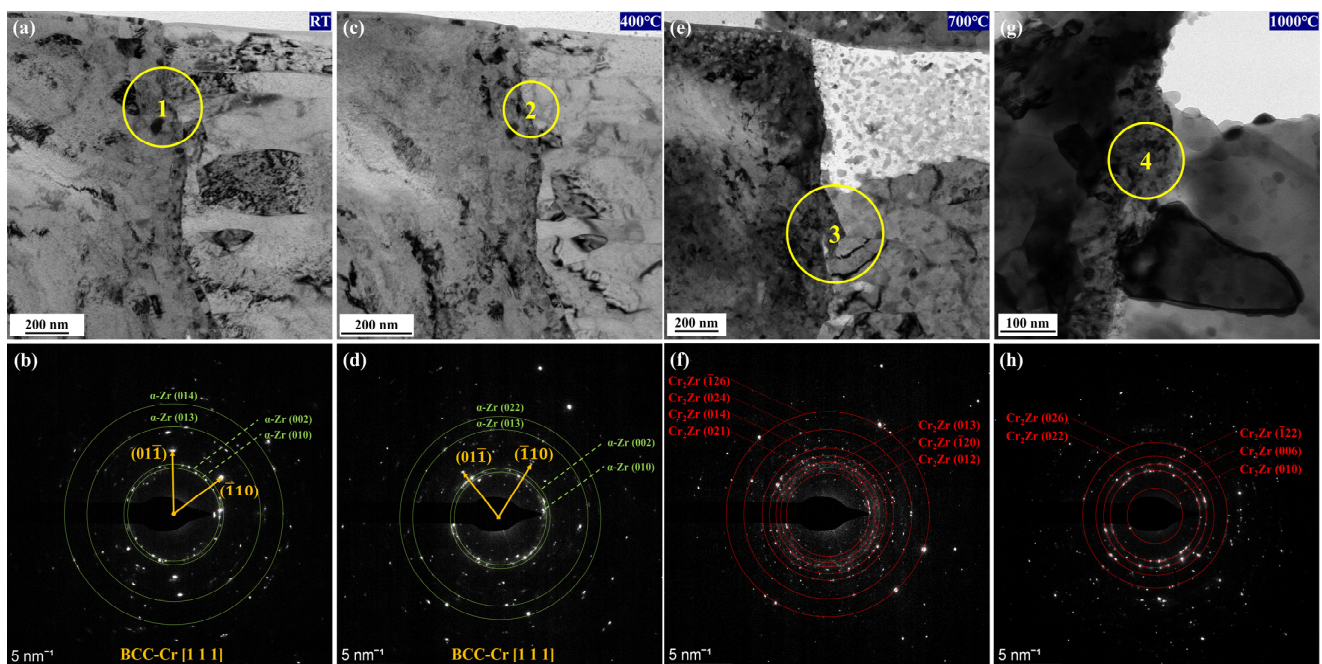
Figure 11. Image of microstructural evolution in the interlayer at high temperatures: (**a**,**b**) RT; (**c**,**d**) 400 °C; (**e**,**f**) 700 °C; and (**g**,**h**) 1000 °C. **b** is the electron diffraction pattern of region 1 in **a**; **d** is the electron diffraction pattern of region 2 in **c**; **f** is the electron diffraction pattern of region 3 in **e**; **h** is the electron diffraction pattern of region 4 in **g**.

A temperature of 700 °C: C14-Cr$_2$Zr#65-3576, a = 5.089 b = 5.089 c = 8.279, α = 90 β = 90 γ = 120, HCP, P63/mmc (194);

A temperature of 1000 °C: C14-Cr$_2$Zr#97-010-8159, a = 5.11 b = 5.11 c = 16.56, α = 90 β = 90 γ = 120, HCP, P63/mmc (194).

The original void disappearance is due to the volume expansion of forming Cr$_2$Zr (the yellow region in Figures 11e,g and 12). The expansion of the Cr$_2$Zr embrittle phase at high temperatures and the thickness increase in the intermetallic layer can easily lead to cracking from the interlayer, which eventually results in Cr coating failure.
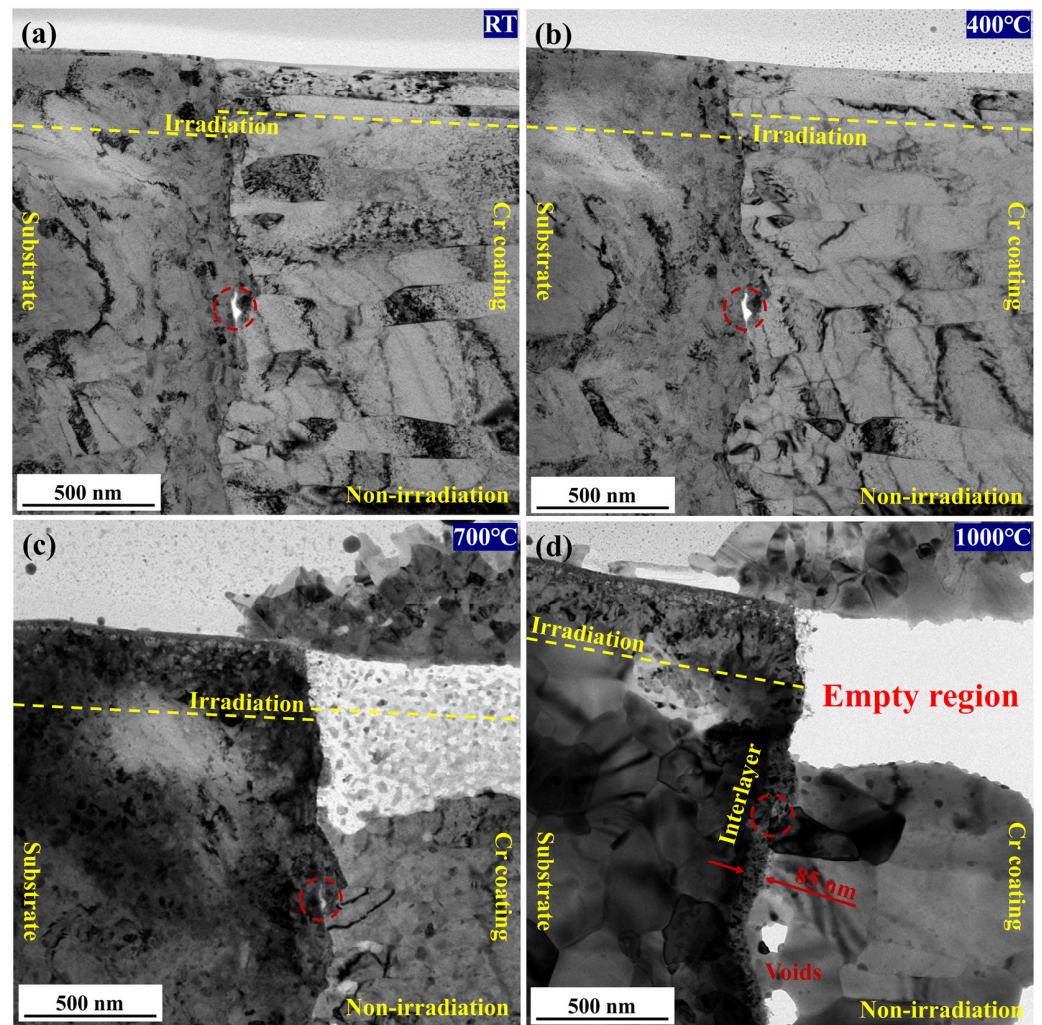

Figure 12. BF of interlayer under different temperatures: (**a**) RT; (**b**) 400 °C; (**c**) 700 °C; and (**d**) 1000 °C.

The sample was in a vacuum environment because the experiment was carried out on the TEM-combined in situ heating rod, i.e., only the Cr-coated Zr-4 interdiffusion in the experiment is without the formation of an oxide layer. We observed that the intermetallic layer thickness was not uniform (Figure 12d), which could be related to the interlayer unevenness or voids in the interlayer, and the grain boundaries provided a fast diffusion channel.

According to video 2 of the in situ TEM heating test, voids appear at the interlayer under a preservation temperature of 700 °C for about 130 s (Figure 7), which could be related to the recrystallization of the Cr coating and the diffusion of Cr. Subsequently, obvious morphology changes in the Zr-4 region close to the interlayer are observed at about 900 °C, as well as the grain refinement region at the interlayer that formed at 1000 °C for preservation about 80 s, which should be the intermetallic phase generated via the reaction of Cr and Zr. With the prolongation of the preservation time, the intermetallic

layer thickness gradually increases, and the thickness growth rate slows down after 10 min of preservation (Figure 13). The phenomena are consistent with the study results of Yang et al. [21] and Xiang et al. [37] because the diffusion coefficient of Cr in the interlayer is five magnitude orders smaller than that in Zr-4, indicating that the diffusion rate of Cr atoms in the interlayer is slower than in Zr-4, and as the intermetallic layer thickens, especially as the solubility and diffusion rate of Cr in Zr-4 increases, it causes the phase transition of the Zr-4 at high temperature, resulting in a gradual slowdown in the growth rate of the interlayer thickness. The growth rate of the interlayer is also related to the coating preparation process, and by comparing the growth rates of the interlayer in coating prepared via magnetron sputtering, multi-arc ion plating, and cold spraying [21,38], the growth rate of the interlayer in coating prepared via multi-arc ion plating is the slowest, that is, has a better diffusion resistance, whereas the method of cold spraying is the fastest. The study of Yang et al. [21] indicated that the growth behavior of the Cr-coated Zr-4 interlayer in a high-temperature inert gas environment was divided into two stages: (1) due to the diffusion and dissolution of Cr atoms in the Zr-4, the thickness of the interlayer gradually increases and eventually reaches a dynamic equilibrium of growth and decomposition; (2) Cr atoms kept diffusing and dissolving into the Zr-4, and eventually, the Cr coating and the interlayer disappeared. However, no stage II was found in this study. A possible reason for this is that the sample sizes used in this study were smaller than others or had insufficient thermal preservation times.
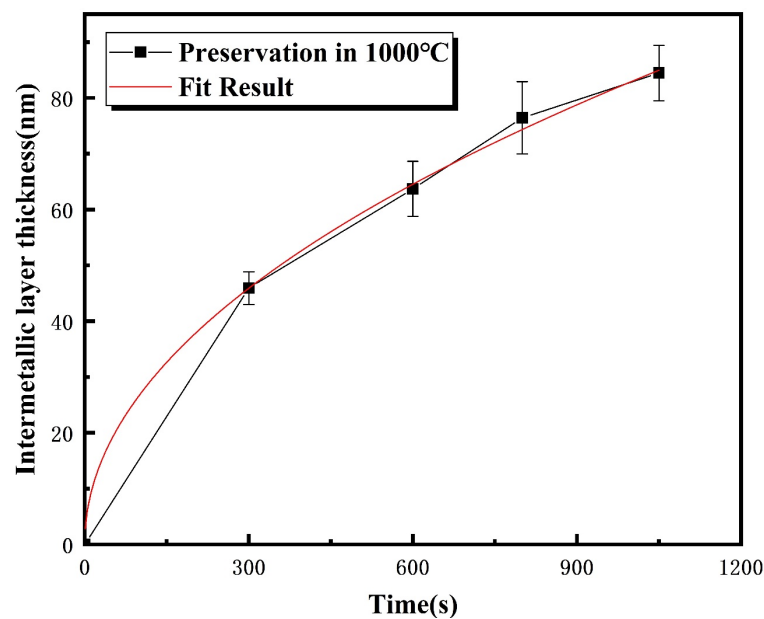
Figure 13. The intermetallic layer thickness (nm) over time(s) under preservation temperature at 1000 °C.

4. Conclusions

In this study, the Cr-Zr interface evolution under continuous heating temperatures from room temperature to 1000 °C was studied using TEM. The following conclusions are obtained based on the in situ heating test of the Cr-Zr interface and subsequent analyses:

(1) Krypton atoms gradually migrated and aggregated at 700 °C to form krypton bubbles and grew with increasing temperature. The reason is the Kr^+ ions introduced via irradiation were trapped by vacancies or vacancy clusters and then became krypton atoms, gradually aggregated at high temperatures. The krypton bubbles as the defects, which were introduced via irradiation, caused grain refinement and stress generation in the irradiation region.

(2) The phenomenon of the irradiation region in Zr-4 changing with temperature is very interesting. As the temperature increased and the preservation time prolonged,

we observed the following phenomena: (a) grain refinement, for which a possible reason is that ion irradiation introduced defects such as interstitials and then grew in a nucleus at high temperatures; (b) grain coarsening due to grain growth at high temperature; (c) grain refinement due to recrystallization, which could be related to residual defects that were introduced via irradiation; and (d) grain growth in the form of columnar crystals.

(3) The irradiation accelerating the Cr coating failure was observed compared with the unirradiated one at the same temperature and preservation time.

(4) The grain coarsening phenomena were observed in the unirradiated region of both Cr coating and Zr-4, which is due to recovery, recrystallization, grain growth, and eventually its growth to equiaxed crystals. The difference in the substrate-irradiated region is that it does not grow in a columnar growth mode.

(5) The Zr-4 and interlayer region formed the Cr_2Zr intermetallic phase (hcp, C14) at both 700 °C and 1000 °C, but the lattice parameters of the intermetallic phase formed at two temperatures were different. With the temperatures increasing, the lattice parameters (c axis) increased, and the lattice expanded. In other words, lattice expansion is present in the Cr coating and interlayer. On the other hand, considering the Zr-4 phase transition, the interlayer is prone to eventually cracking during the cooling process, resulting in Cr coating failure.

Author Contributions: Y.Z.: Methodology, Software, Data curation, Writing—original draft. X.W.: Investigation. L.W.: Investigation. S.Z.: Investigation. H.S.: Investigation. Z.N.: Investigation. W.Z.: Investigation. N.L.: Investigation. J.Y.: Writing—review & editing, Supervision. All authors have read and agreed to the published version of the manuscript.

Institutional Review Board Statement: Not applicable.

Informed Consent Statement: Not applicable.

Data Availability Statement: Not applicable.

Conflicts of Interest: The authors declare no conflict of interest.

References

1. Brachet, J.C.; Lorrette, C.; Michaux, A.; Sauder, C.; Idarraga-Trujillo, I.; Le Saux, M.; Le Flem, M.; Schuster, F.; Billard, A.; Monsifrot, E.; et al. CEA studies on advanced nuclear fuel claddings for enhanced accident tolerant LWRs fuel (LOCA and beyond LOCA conditions). In Proceedings of the Fontevraud 8—Contribution of Materials Investigations and Operating Experience to Lwrs' Safety, Performance and Reliability, Avignon, France, 15–18 September 2014.
2. Schuster, F.; Lomello, F.; Billard, A.; Velisa, G.; Monsifrot, E.; Bischoff, J.; Ambard, A.; Brachet, J.C.; Lesaux, M.; Leflem, M.; et al. On-going studies at CEA on chromium coated zirconium based nuclear fuel claddings for enhanced accident tolerant LWRs fuel. In Proceedings of the TopFuel 2015—Reactor Fuel Performance Meeting, Zurich, Switzerland, 13–15 September 2015.
3. Brachet, J.C.; Le Saux, M.; Lezaud-Chaillioux, V.; Dumerval, M.; Houmaire, Q.; Lomello, F.; Schuster, F.; Monsifrot, E.; Bischoff, J.; Pouillier, E. Behavior under LOCA conditions of Enhanced Accident Tolerant Chromium Coated Zircaloy-4 Claddings. In Proceedings of the Topfuel 2016—Light Water Reactor (LWR) Fuel Performance Meeting, Boise, ID, USA, 11–16 September 2016.
4. Kashkarov, E.; Afornu, B.; Sidelev, D.; Krinitcyn, M.; Gouws, V.; Lider, A. Recent Advances in Protective Coatings for Accident Tolerant Zr-Based Fuel Claddings. *Coatings* **2021**, *11*, 557. [CrossRef]
5. Tang, C.; Stueber, M.; Seifert, H.J.; Steinbrueck, M. Protective coatings on zirconium-based alloys as accident-tolerant fuel (ATF) claddings. *Corros. Rev.* **2017**, *35*, 141–165. [CrossRef]
6. Ko, J.; Kim, J.W.; Min, H.W.; Kim, Y.; Yoon, Y.S. Review of manufacturing technologies for coated accident tolerant fuel cladding. *J. Nucl. Mater.* **2022**, *561*, 153562. [CrossRef]
7. Brachet, J.-C.; Idarraga-Trujillo, I.; Flem, M.L.; Saux, M.L.; Vandenberghe, V.; Urvoy, S.; Rouesne, E.; Guilbert, T.; Toffolon-Masclet, C.; Tupin, M.; et al. Early studies on Cr-Coated Zircaloy-4 as enhanced accident tolerant nuclear fuel claddings for light water reactors. *J. Nucl. Mater.* **2019**, *517*, 268–285. [CrossRef]
8. Yang, J.; Steinbrück, M.; Tang, C.; Große, M.; Liu, J.; Zhang, J.; Yun, D.; Wang, S. Review on chromium coated zirconium alloy accident tolerant fuel cladding. *J. Alloys Compd.* **2022**, *895*, 162450. [CrossRef]

9. Chen, Q.S.; Liu, C.H.; Zhang, R.Q.; Yang, H.Y.; Wei, T.G.; Wang, Y.; Li, Z.; He, L.X.; Wang, J.; Wang, L.; et al. Microstructure and high-temperature steam oxidation properties of thick Cr coatings prepared by magnetron sputtering for accident tolerant fuel claddings: The role of bias in the deposition process. *Corros. Sci.* **2020**, *165*, 108378. [CrossRef]

10. Park, J.-H.; Kim, H.-G.; Park, J.-y.; Jung, Y.-I.; Park, D.-J.; Koo, Y.-H. High temperature steam-oxidation behavior of arc ion plated Cr coatings for accident tolerant fuel claddings. *Surf. Coat. Technol.* **2015**, *280*, 256–259. [CrossRef]

11. Han, X.; Xue, J.; Peng, S.; Zhang, H. An interesting oxidation phenomenon of Cr coatings on Zry-4 substrates in high temperature steam environment. *Corros. Sci.* **2019**, *156*, 117–124. [CrossRef]

12. Hu, X.; Dong, C.; Wang, Q.; Chen, B.; Yang, H.; Wei, T.; Zhang, R.; Gu, W.; Chen, D. High-temperature oxidation of thick Cr coating prepared by arc deposition for accident tolerant fuel claddings. *J. Nucl. Mater.* **2019**, *519*, 145–156. [CrossRef]

13. Kim, H.-G.; Kim, I.-H.; Jung, Y.-I.; Park, D.-J.; Park, J.-Y.; Koo, Y.-H. Adhesion property and high-temperature oxidation behavior of Cr-coated Zircaloy-4 cladding tube prepared by 3D laser coating. *J. Nucl. Mater.* **2015**, *465*, 531–539. [CrossRef]

14. Yang, J.H.; Song, K.W.; Kim, K.S.; Jung, Y.H. A fabrication technique for a UO_2 pellet consisting of UO_2 grains and a continuous W channel on the grain boundary. *J. Nucl. Mater.* **2006**, *353*, 202–208. [CrossRef]

15. Kim, D.-J.; Rhee, Y.W.; Kim, J.H.; Kim, K.S.; Oh, J.S.; Yang, J.H.; Koo, Y.-H.; Song, K.-W. Fabrication of micro-cell UO_2–Mo pellet with enhanced thermal conductivity. *J. Nucl. Mater.* **2015**, *462*, 289–295. [CrossRef]

16. Hwang, D.H.; Hong, S.G.; In, W.K. A Comparative Physics Study of Commercial PWR Cores using Metallic Micro-cell UO_2-Cr (or Mo) Pellets with Cr-based Cladding Coating. In Proceedings of the Transactions of the Korean Nuclear Society Spring Meeting, Jeju, Korea, 12–13 May 2016.

17. Jeong, E.; Jo, Y.; Shin, C.; Yang, Y.-S.; Kim, J.-Y.; Lee, D. Performance analysis of nuclear reactor core loaded with Accident-Tolerant Fuel: Mo/Cr metallic microcell UO_2 pellets and CrAl coating. *Ann. Nucl. Energy* **2022**, *175*, 109217. [CrossRef]

18. Koo, Y.-H.; Yang, J.-H.; Park, J.-Y.; Kim, K.-S.; Kim, H.-G.; Kim, D.-J.; Jung, Y.-I.; Song, K.-W. KAERI's Development of LWR Accident-Tolerant Fuel. *Nucl. Technol.* **2017**, *186*, 295–304. [CrossRef]

19. Jiang, H.; Duan, Z.; Zhao, X.; Zhang, B.; Wang, P. Influence of ions irradiation on the microstructural evolution, mechanical and tribological properties of Zr-4 alloy. *Appl. Surf. Sci.* **2019**, *498*, 143821. [CrossRef]

20. Jiang, J.-S.; Wang, D.-Q.; Du, M.-Y.; Ma, X.-F.; Wang, C.-X.; He, X.-J. Interdiffusion behavior between Cr and Zr and its effect on the microcracking behavior in the Cr-coated Zr-4 alloy. *Nucl. Sci. Tech.* **2021**, *32*, 134. [CrossRef]

21. Yang, J.; Stegmaier, U.; Tang, C.; Steinbrück, M.; Große, M.; Wang, S.; Seifert, H.J. High temperature Cr-Zr interaction of two types of Cr-coated Zr alloys in inert gas environment. *J. Nucl. Mater.* **2021**, *547*, 152806. [CrossRef]

22. Ma, H.-B.; Yan, J.; Zhao, Y.-H.; Liu, T.; Ren, Q.-S.; Liao, Y.-H.; Zuo, J.-D.; Liu, G.; Yao, M.-Y. Oxidation behavior of Cr-coated zirconium alloy cladding in high-temperature steam above 1200 °C. *npj Mater. Degrad.* **2021**, *5*, 7. [CrossRef]

23. Huang, J.; Zou, S.; Xiao, W.; Yang, C.; Yu, H.; Zhang, L.; Zhang, K. Microstructural evolution of Cr-coated Zr-4 alloy prepared by multi-arc ion plating during high temperature oxidation. *J. Nucl. Mater.* **2022**, *562*, 153616. [CrossRef]

24. Jiang, J.; Du, M.; Pan, Z.; Yuan, M.; Ma, X.; Wang, B. Effects of oxidation and inter-diffusion on the fracture mechanisms of Cr-coated Zry-4 alloys: An in situ three-point bending study. *Mater. Des.* **2021**, *212*, 110168. [CrossRef]

25. Wei, T.; Zhang, R.; Yang, H.; Liu, H.; Qiu, S.; Wang, Y.; Du, P.; He, K.; Hu, X.; Dong, C. Microstructure, corrosion resistance and oxidation behavior of Cr-coatings on Zircaloy-4 prepared by vacuum arc plasma deposition. *Corros. Sci.* **2019**, *158*, 108077. [CrossRef]

26. Kuprin, A.S.; Vasilenko, R.L.; Tolstolutskaya, G.D.; Voyevodin, V.N.; Belous, V.A.; Ovcharenko, V.D.; Kopanets, I.E. Irradiation resistance of chromium coatings for ATFC in the temperature range 300–550 °C. *J. Nucl. Mater.* **2021**, *549*, 152908. [CrossRef]

27. Jiang, L.; Xiu, P.; Yan, Y.; Lu, C.; Huang, M.; Liu, T.; Ye, C.; Sun, H.; Shu, R.; Wang, L. Effects of ion irradiation on chromium coatings of various thicknesses on a zirconium alloy. *J. Nucl. Mater.* **2019**, *526*, 151740. [CrossRef]

28. Maier, B.R.; Yeom, H.; Johnson, G.; Dabney, T.; Hu, J.; Baldo, P.; Li, M.; Sridharan, K. In situ TEM investigation of irradiation-induced defect formation in cold spray Cr coatings for accident tolerant fuel applications. *J. Nucl. Mater.* **2018**, *512*, 320–323. [CrossRef]

29. Huang, M.; Li, Y.; Ran, G.; Yang, Z.; Wang, P. Cr-coated Zr-4 alloy prepared by electroplating and its in situ He^+ irradiation behavior. *J. Nucl. Mater.* **2020**, *538*, 152240. [CrossRef]

30. Wang, R.; Li, P.; Li, B.; Hu, L.; Huang, F.; Huang, Q.; Ge, F. The oxidation mechanisms of the Xe^{20+} ion-irradiated Cr coatings on Zr alloy coupons: Accelerated diffusion and internal oxidation. *Corros. Sci.* **2022**, *201*, 110301. [CrossRef]

31. Wu, A.; Ribis, J.; Brachet, J.C.; Clouet, E.; Leprêtre, F.; Bordas, E.; Arnal, B. HRTEM and chemical study of an ion-irradiated chromium/zircaloy-4 interface. *J. Nucl. Mater.* **2018**, *504*, 289–299. [CrossRef]

32. Kuprin, A.S.; Belous, V.A.; Voyevodin, V.N.; Vasilenko, R.L.; Ovcharenko, V.D.; Tolstolutskaya, G.D.; Kopanets, I.E.; Kolodiy, I.V. Irradiation resistance of vacuum arc chromium coatings for zirconium alloy fuel claddings. *J. Nucl. Mater.* **2018**, *510*, 163–167. [CrossRef]

33. Ni, K.; Ma, Q.; Wan, H.; Yang, B.; Ge, J.; Zhang, L.; Si, N. Effect of He^+ fluence on surface morphology and ion-irradiation induced defect evolution in 7075 aluminum alloys. *Mater. Res. Express* **2018**, *5*, 026514. [CrossRef]

34. Zhang, X.; Mei, X.; Cao, X.; Wang, Y.; Sun, J.; Zheng, P. The effect of He ions irradiation on the micro-structure and property of CLF-1 steel. *J. Nucl. Mater.* **2018**, *509*, 496–503. [CrossRef]

35. He, L.F.; Valderrama, B.; Hassan, A.R.; Yu, J.; Gupta, M.; Pakarinen, J.; Henderson, H.B.; Gan, J.; Kirk, M.A.; Nelson, A.T.; et al. Bubble formation and Kr distribution in Kr-irradiated UO_2. *J. Nucl. Mater.* **2015**, *456*, 125–132. [CrossRef]

36. Ran, G.; Xu, J.; Shen, Q.; Zhang, J.; Li, N.; Wang, L. In situ TEM observation of growth behavior of Kr bubbles in zirconium alloy during post-implantation annealing. *Nucl. Instrum. Methods Phys. Res. Sect. B Beam Interact. Mater. At.* **2013**, *307*, 516–521. [CrossRef]
37. Wenxin, X.; Shihao, Y. *Reaction Diffusion in Chromium-Zircaloy-2 System*; China Nuclear Information Centre: Beijing, China, 2001.
38. He, X.; Tian, Z.; Shi, B.; Xu, X.; Meng, C.; Dang, W.; Tan, J.; Ma, X. Effect of gas pressure and bias potential on oxidation resistance of Cr coatings. *Ann. Nucl. Energy* **2019**, *132*, 243–248. [CrossRef]